Optimum Design of the Current-Source Flyback Inverter for Decentralized Grid-Connected Photovoltaic Systems

A. Ch. Kyritsis, *Student Member, IEEE*, E. C. Tatakis, and N. P. Papanikolaou

***Abstract*—Two alternative modes of operation for the current-source flyback inverter are investigated in this paper. The discontinuous conduction mode (DCM), where a constant switching frequency (CSF) control method is applied, and the boundary between continuous and DCM (BCM) that is introduced for photovoltaic (PV) applications in this paper (where a variable switching frequency control method is applied). These two control methods are analytically studied and compared in order to establish their advantages as well as their suitability for the development of an inverter for decentralized grid-connected PV applications. An optimum design methodology is developed, aiming for an inverter with the smallest possible volume for the maximum power transfer to the public grid and wide PV energy exploitation. The main advantages of the current-source flyback inverter are very high-power density and high efficiency due to its simple structure, as well as high-power factor regulation. The design and control methodology are validated by personal computer simulation program with integrated circuit emphasis (PSPICE) simulation and experimental results, accomplished on a laboratory prototype.**

***Index Terms*—Current-source inverter, dc–ac power conversion, design methodology, distributed generation, photovoltaics (PVs), single-phase grid-connected inverter.**

NOMENCLATURE

BCM	Boundary (between continuous and discontinuous) conduction mode.
CSF	Constant switching frequency.
DCM	Discontinuous conduction mode.
d	Duty cycle of the primary semiconductor switch.
d_p	Duty cycle value referring to the switching cycle that occurs at the time-area of $\omega t = \pi/2$.
f_S	Switching frequency of the primary switch (kHz).
$f_{s,\max}$	Maximum switching frequency value of the primary switch for the BCM (kHz).
$f_{s,\min}$	Minimum switching frequency value of the primary switch for the BCM (kHz).
$f_{s,\text{avg}}$	Average switching frequency value of the primary switch for the BCM (kHz).
eff	Inverter efficiency.
g_S	Current-source conductivity (Ω^{-1}).
g_L	$= 1/f_s L_1 (\Omega^{-1})$.
$g_{\text{L,avg}}$	$= 1 f_{s,\text{avg}} L_1 (\Omega^{-1})$.
$i_S(t)$	Current-source time function (A).
$i_{\text{dc}}(t)$	Transformer primary winding current time function (A).
$I_{\text{dc,avg}}$	Average value of the primary transformer winding current (A).
$i_{\text{dc,p}}$	Transformer primary winding peak current value for a switching cycle (A).
L_1	Transformer primary inductance (μH).
n	Transformer turns ratio value.
N_{ac}	Number of turns of the transformer secondary winding (ac-side).
N_{dc}	Number of turns of the transformer primary winding (PV-side).
P_{ac}	Power that is transferred to the ac grid (W).
P_{dc}	DC stage processed power (W).
pf	Power factor at the mains side after filtering.
T_S	Switching period of the primary switch (s).
T_{hl}	Rectified line period (s).
$T_{s,\max}$	Maximum switching period of the primary switch for the BCM (s).
$T_{s,\min}$	Minimum switching period of the primary switch for the BCM (s).
$T_{s,\text{avg}}$	Average switching period of the primary switch for the BCM (s).
t_{on}	Primary switch on-time (s).
$t_{\text{on},p}$	t_{on} interval value referring to the switching cycle that occurs at the time-area of $\omega t = \pi/2$ (s).
t_{off}	Primary switch off-time (s).
$u_{\text{ac}}(t)$	Mains voltage time function (V).
$V_{\text{ac},p}$	Peak mains voltage value (V).
$V_{\text{ac,rms}}$	RMS value of the mains voltage (V).
V_{dc}	PV generator voltage value at the maximum power point (V).
VSF	Variable switching frequency.
$V_{S1,p}$	Peak voltage stress of the primary switch (V).
$V_{S2,p}$	Peak voltage stress of the switches at the mains side (V).
w	Integer part of T_{hl}/T_s.
λ	Ratio $V_{\text{dc}}/V_{\text{ac,p}}$.
θ	$= \omega t$.
ω	Mains angular frequency (rad/s).

Manuscript received December 22, 2005; revised July 6, 2006. This work is supported in part by the European Social Fund (75%), in part by the Greek General Secretariat Research and Technology (25%), and in part by the ANCO S.A. and Energy Solutions S.A. within the framework of Measure 8.3 of the Operational Programme "Competitiveners" and 3rd Community Support Programme (PENED 03400). Paper no. TEC-00004-2005.

A. Ch. Kyritsis and E. C. Tatakis are with the Department of Electrical and Computer Engineering, Laboratory of Electromechanical Energy Conversion, University of Patras, Rion-Patras 26504, Greece (e-mail: Kyritsis@ece.upatras.gr; E.C.Tatakis@ece.upatras.gr).

N. P. Papanikolaou is with the Hellenic Transmission System Operator (HTSO) S.A., N. Smyrni 17122, Greece (e-mail: Npapanikolaou@desmie.gr).

Digital Object Identifier 10.1109/TEC.2007.895854

I. Introduction

As MANY countries have ratified the Kyoto Accord aiming at a reduction of gas emissions, there is a growing recognition of the role that solar power can play in the battle to reduce carbon dioxide levels. Nowadays, there are two potential markets for electric power generation from photvoltaic (PV) systems: large-scale power plants sized up to several megawatts (large-scale electricity generation in desert regions with high insolation, PV stand-alone or grid-connected systems for professional use, etc.) and small-scale residential applications, where the power production usually varies between 0.1 and 5 kW [1]–[3]. The residential applications can be used either as stand-alone systems, where there is no access to the utility grid (electrification of remote villages and islands, water pumping in developing countries, etc.), or as grid-connected systems (grid-connected PV building) [2]–[4]. In this case, the grid acts as a battery bank with an unlimited storage capacity. Therefore, the total generation capability of a decentralized grid-connected PV system will be better than that of a stand-alone system; as there is virtually no limit to the storage capacity, the generated electricity can always be stored, whereas in stand-alone applications, the batteries of the PV system will be sometimes fully loaded, and therefore, the generated electricity has to be "thrown away."

Since the implementation of large-scale PV power plants is not cost-effective yet, the use of several decentralized grid-connected PV systems is quite more appropriate as they can also be easily installed on buildings [3].

The latest technology on decentralized grid-connected PV systems is the so-called "ac–PV module" [5]–[8]. An ac–PV module is the combination of a single PV module and a single-phase power electronic inverter. The inverter is mounted either on the rear side of the module or on the support structure and is directly connected to the PV module. The benefits of this approach are not only the lack of power loss, due to mismatch between the PV modules, but also the lack of dc connections, arcs, and ground faults [7]. The concept of ac–PV module supports optimal adjustment between the PV module and the inverter, which may lead to an overall better performance. Beyond that, the installed power can be easily upgraded. Moreover, it has the possibility to become a "buy n plug" device that can be installed even by untrained individuals. The power process unit of these systems is usually a single-phase controllable power converter, ranging from 50–350 W. The selection of the appropriate converter topology has to take into account the following requirements:

- high efficiency and high-power density;
- low cost and high reliability;
- compliance with the electromagnetic compatibility (EMC) directives and low-voltage regulations [9];
- IEEE 929-2000 Standard—IEEE Recommended Practice for Utility Interface of Photovoltaic Systems;
- IEEE 1547 Standard for Interconnecting Distributed Resources with the Electric Power System.

The dc-to-ac voltage conversion can be implemented by any single-step or multistep topology [5]–[8], [10]. As it has been shown in [11]–[14], the so-called flyback inverter is rather an attractive solution. As mentioned in these papers, the inverter operates in DCM. So, it has to behave as a current source whose value depends on the mains voltage. However, an analytical design procedure, which will ensure high-power density and wide exploitation of PV-generated power has not been presented before.

Concerning the voltage-controlled current-source modification requirement, it is obvious that the inverter cannot operate in continuous conduction mode—where the transformer is incompletely discharged during a switching cycle—because in this case, it will become a load-independent voltage source. Thus, two operation modes can be used: the one already presented in [11]–[14] (DCM) as well as the boundary between continuous and discontinuous (BCM) that is introduced for PV applications in this paper.

In the following sections, both DCM and BCM modes of operation will be analytically investigated and compared in order to establish their suitability for the development of an inverter with the smallest possible volume for a given power level. By this investigation, the operational limitations of both operation modes will be emerged. Finally, an optimal design strategy for wide PV-generated power exploitation is proposed for daily energy production maximization.

The inverter will be studied without the presence of a maximum power point tracking (MPPT) control and an islanding detection scheme, since the aim of this paper is to investigate the efficiency, the total harmonic distortion (THD) reduction, and the power density that this inverter performs under any line and load conditions. Various MPPT control methods [14], [15] and islanding detection schemes [16], [17] could be adopted for the case of the flyback current-source inverter in both modes of operation.

II. Voltage-Controlled Current-Source Modification Requirement

The basic idea of developing a flyback current-source inverter for energy transfer from a PV system to the mains is to modify a current source whose value depends on the mains voltage

$$i_{\mathrm{S}}(t) = g_{\mathrm{S}} u_{\mathrm{ac}}(t) \tag{1}$$

$$u_{\mathrm{ac}}(t) = V_{\mathrm{ac,p}} \sin \omega t. \tag{2}$$

As shown in Fig. 1, this inverter performs energy flow from the dc to the ac stage by using two identical secondary windings. Each of them is able to transfer energy to the ac side during a line half cycle. For this reason, two controllable switches are placed between these windings and the mains side. Both of them are appropriately controlled by the mains voltage, so as to conduct during a line half cycle. Thus, assuming that the L_f voltage drop as well as the C_f 50-Hz harmonic current are negligible, for each line half cycle, the equivalent circuit is that of Fig. 2(a), and therefore, the system operates as a dc/dc flyback converter with variable output voltage.

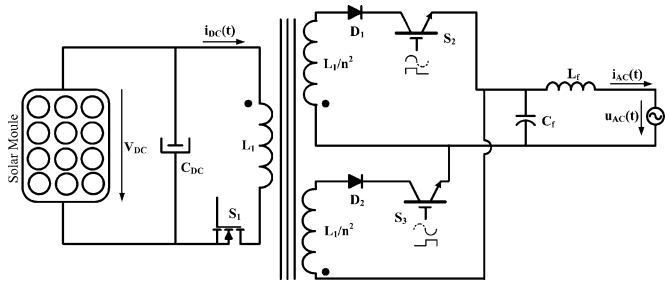

Fig. 1. High-frequency single-stage current-source flyback inverter.

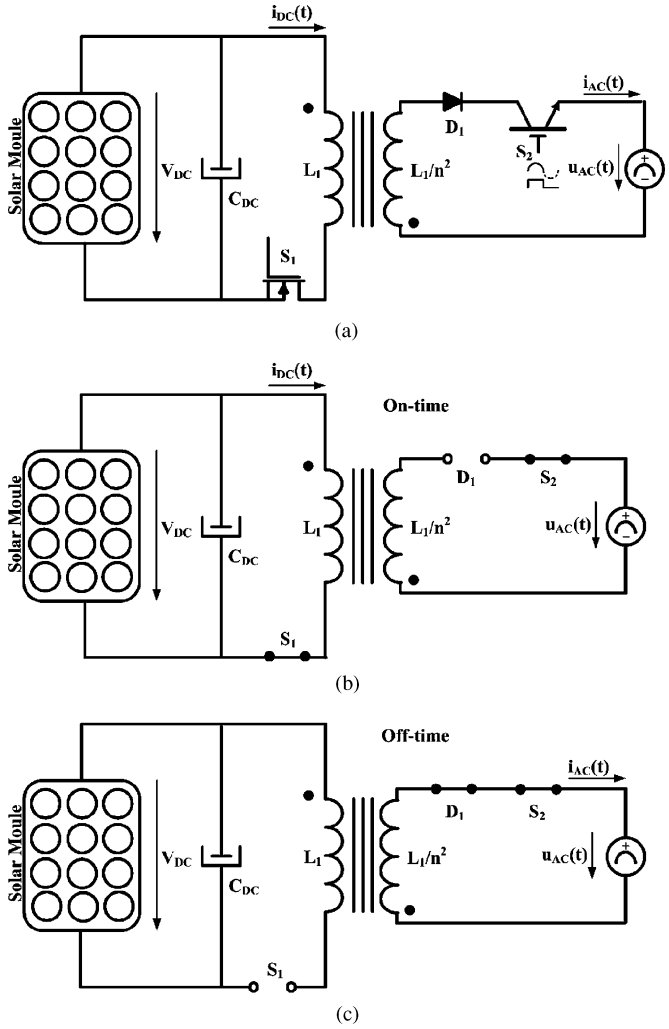

Fig. 2. Equivalent circuit of the current-source flyback inverter during a line half cycle. (a) Each line half cycle. (b) During S_1 on-time. (c)During S_1 off-time.

III. Basic Analysis of the DCM Operation

In this section, the DCM operation will be analytically investigated in order to conclude to its optimal design scheme. This operation mode has been widely used in ac–PV module applications mainly due to its simplicity (eclipse of high-frequency current measure). Nevertheless, due to the unavoidable dead-times on the transformer current feed, its use is limited to small power levels.

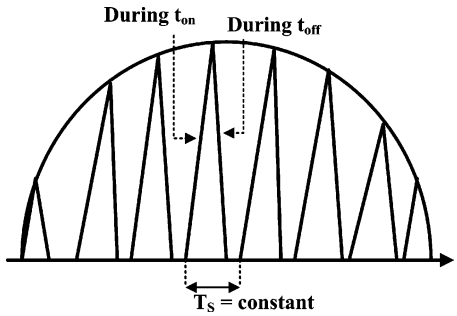

Fig. 3. Transformer current representation for the case of DCM operation where constant switching frequency control method is applied.

The main idea of this technique is to "force" the peak current value of each switching cycle to become proportional to the sinusoidal mains voltage. Fig. 3 shows the equivalent transformer current waveform.

Obviously, when S_1 conducts [$t_{\rm on}$ interval, Fig. 2(b)], this current flows through the primary winding, while when S_1 is off, it flows through the "active" secondary winding [$t_{\rm off}$ interval—diode conducts; Fig. 2(c)]. Finally, during the time interval between the complete transformer discharge and the beginning of a new switching cycle, there is no current flow through the transformer. During on-time, the equivalent circuit is that of Fig. 2(b) (S_1 is on and D_1 is off), and the transformer current can be calculated according to the following equation:

$$V_{\rm dc} = L_1 \frac{{\rm d}i_{\rm dc}(t)}{{\rm d}t}. \tag{3}$$

Thus, the peak current value for a switching cycle is

$$i_{{\rm dc},p} = \frac{V_{\rm dc}}{L_1} t_{\rm on}. \tag{4}$$

Using the duty cycle $d = t_{\rm on}/T_S$ parameter, (4) can be rewritten as

$$i_{{\rm dc},p} = \frac{V_{\rm dc}}{L_1 f_s} d. \tag{5}$$

Since the peak transformer current value should have a sinusoidal waveform

$$i_{{\rm dc},p}(t) = I_{{\rm dc},p} \sin \omega t, \quad \omega t \in [0, \pi] \tag{6}$$

we can conclude that the duty cycle has to be modified in such a way, so as to become

$$d(t) = d_p \sin \omega t \tag{7}$$

where d_p is the duty cycle value referring to the switching cycle that occurs at the time-area of $\omega t = \pi/2$.

The exact value of d_p is determined by the desired output power level of the PV generator by using a reference signal. Thus, in DCM operation, where the switching frequency remains constant (CSF), the block diagram of the control circuit is a simple pulse width modultaion (PWM) loop, as shown in Fig. 4.

The transformer turns ratio value n, where n is

$$n = \frac{N_{\rm dc}}{N_{\rm ac}} \tag{8}$$

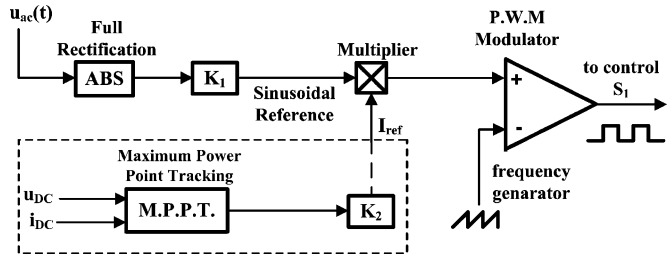

Fig. 4. Block diagram of the control circuit for the DCM operation (constant switching frequency).

has to be appropriately selected so as to reassure that the inverter will always be in DCM. Thus, it has to be confirmed that the $t_{\rm off}$ interval is smaller than the time interval between the switching period and the $t_{\rm on}$ interval for the maximum power level

$$t_{\rm off} \leq T_s - t_{{\rm on},p}. \tag{9}$$

The calculation of $t_{\rm off}$ can be done by using the equivalent circuit of Fig. 2(c) (S_1 is off, S_2 is on, and D_1 is on)

$$u_{\rm ac}(t) = \frac{{\rm d}\left[n i_{\rm dc}(t)\right]}{{\rm d}t}\frac{L_1}{n^2}. \tag{10}$$

Since the switching period is much smaller than the line period, we can assume that $u_{\rm ac}(t)$ remains almost constant during a switching cycle. According to (10)—taking for granted that the transformer current becomes zero at the end of $t_{\rm off}$ interval—we can express $t_{\rm off}$ as (see Appendix A)

$$\frac{t_{\rm off}}{T_s} = \frac{\lambda}{n} d_p = \text{constant} \tag{11}$$

for any switching period within the line half cycle, where

$$\lambda = \frac{V_{\rm dc}}{V_{{\rm ac},p}}. \tag{12}$$

Combining (9) and (11), we can conclude to the following DCM criterion:

$$d_p \leq \frac{1}{1+\frac{\lambda}{n}}. \tag{13}$$

A. Investigation of the Power Density for DCM

After the basic theoretical analysis of the DCM operation, where constant frequency control technique is applied, it is essential to investigate the inverter-transferred power density in relation with its operation parameters, so as to result in a minimum inverter structure of high efficiency. Assuming that the inverter has unitary efficiency and that the primary and secondary transformer leakage inductances are negligible, the power that is transferred to the power network $P_{\rm ac}$ is equal to the power of the dc stage $P_{\rm dc}$

$$P_{\rm ac} = P_{\rm dc} = P. \tag{14}$$

Considering that the inverter is in steady state, we can express the transferred power as

$$P = V_{\rm dc} I_{\rm dc,avg} \tag{15}$$

$$I_{\rm dc,avg} = \frac{1}{T_{hl}} \int_0^{T_{hl}} i_{\rm dc}(t){\rm d}t. \tag{16}$$

The above integral can be rewritten as

$$I_{\rm dc,avg} = \frac{1}{T_{hl}} \left[\int_0^{T_s} i_{\rm dc}(t){\rm d}t + \cdots + \int_{(w-1)T_s}^{wT_s} i_{\rm dc}(t)\ {\rm d}t + Q \right] \tag{17}$$

where w is the integer part of T_{hl}/T_s and Q is the remaining part of the integral—referring to the beginning or ending of a line half cycle—and hence, it can be neglected.

By using (3), (7), and (17) and taking into account that

$$\omega t = \left(\frac{\pi}{T_{hl}}\right)(iT_s) \approx \frac{\pi}{w} i \tag{18}$$

we can conclude that (see Appendix B)

$$I_{\rm dc,avg} = \frac{d_p^2 V_{\rm dc}}{2 f_s L_1} \left[\frac{1}{w} \sum_{i=1}^{w} \sin^2\left(\frac{\pi}{w} i\right) \right] = \frac{d_p^2 V_{\rm dc}}{4 f_s L_1} = \frac{1}{4} g_L d_p^2 V_{\rm dc} \tag{19}$$

where

$$g_L = \frac{1}{f_s L_1}. \tag{20}$$

Combining (12), (14), and (19), the transferred power becomes

$$P = \frac{1}{4}\frac{d_p^2}{f_s L_1} V_{\rm dc}^2 = \frac{1}{4} d_p^2 g_L V_{\rm dc}^2. \tag{21}$$

Using (12) and (21), we can describe P as

$$P = \frac{1}{2}\frac{\lambda^2 d_p^2}{f_s L_1} V_{\rm ac,rms}^2 = \frac{1}{2}\lambda^2 d_p^2 g_L V_{\rm ac,rms}^2. \tag{22}$$

As it is shown in (1), the fundamental inverter current that flows to the network (after the RF filter) is in phase with the mains voltage. For this reason, we can express the transferred power as

$$P = g_S V_{\rm ac,rms}^2 \tag{23}$$

Combining (21) and (23) we conclude that

$$\frac{g_S}{g_L} = \frac{1}{2}\lambda^2 d_p^2 \tag{24}$$

Thus, according to eq. (13) in order to transfer power while remaining in DCM, the following equation should be fulfilled:

$$\left(\frac{g_s}{g_L}\right)_{\max} = \frac{1}{2}\left(\frac{1}{\lambda} + \frac{1}{n}\right)^{-2} \tag{25}$$

Fig. 5 shows $(g_S/g_L)_{\max}$ as a function of n with λ as parameter.

The range of parameter λ has been selected considering typical mains voltage values and the PV generators voltage values (which are used for "ac–PV module" applications) at the maximum power [18]. In Europe, λ varies between 0.044 and 0.214, and in USA, between 0.088 and 0.428. As it is obvious, for given values of λ and g_L, the transferred power depends strongly on the transformer turns ratio n. However, as n increases, there is saturation on the power increase, and thus, there is an upper

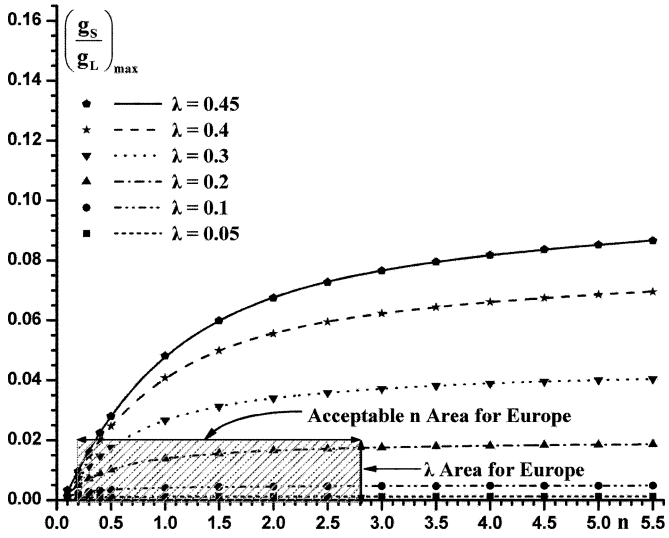

Fig. 5. $(g_S/g_L)_{\max}$ as a function of λ and n for the DCM operation.

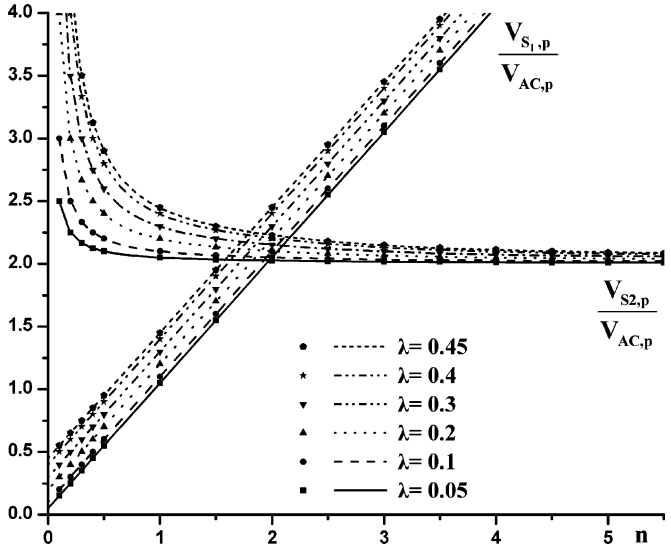

Fig. 6. $V_{S1,p}/V_{\mathrm{ac},p}$ and $V_{S2,p}/V_{\mathrm{ac},p}$ as a function of λ and n, for the DCM operation.

limit for its value. This limit can be calculated from (25) for the case that n-value becomes infinite

$$\left(\frac{g_S}{g_L}\right)_{\max}\Bigg|_{n\to\infty} = \frac{\lambda^2}{2}. \tag{26}$$

The above analysis leads to the following conclusion; for a specific λ value, any operation point, which is located at the area under the corresponding curve of $(g_S/g_L)_{\max}$, is a feasible solution in order to transfer a given power, while remaining in DCM operation. However, according to (13), the best selection of operation points occurs when there is equality, which means that the $(g_S/g_L)_{\max}$ curve points are the optimum ones, leading to the maximum power density.

The appropriate selection of the exact operating point depends on constructional parameters. The way in which the selection of the transformer turns ratio affects the design of the inverter is discussed next.

The transformer turns ratio affects the maximum voltage value across the semiconductor switches. In more detail, by using the equivalent circuit of Fig. 2(c), the voltage stress on the switch at the PV generator side can be calculated according to the following equation:

$$\frac{V_{S_1,p}}{V_{\mathrm{ac},p}} = \lambda + n. \tag{27}$$

Fig. 6 shows $V_{S1,p}/V_{\mathrm{ac},p}$ as a function of n with λ as parameter.

By studying this figure, we conclude that there is a strong limit on the n-value selection. Although, according to Fig. 5, the best n-value selection, for a given λ, is the closest one to the starting point of saturation area; this value may lead to unacceptable large voltage stress on the primary switch S_1.

Concerning the maximum voltage across the semiconductor switches at the mains side, it can be calculated by using the equivalent circuit of Fig. 1

$$\frac{V_{S_2,p}}{V_{\mathrm{ac},p}} = \frac{\lambda}{n} + 2. \tag{28}$$

Additionally, the n-value selection also affects the maximum peak current value on the primary switch S_1, as shown from the combination of (5), (13), and (19)

$$\frac{I_{\mathrm{dc},p}}{I_{\mathrm{dc,avg}}} = 4\left[1 + \frac{\lambda}{n}\right]. \tag{29}$$

By studying the above two equations, we conclude that there is a strong limit on the n-value selection; a small n-value may lead to unacceptable large current value for the primary switch S_1 and to excessive voltage stress on the semiconductor switches S_2, S_3.

Thus, the exact n-value that has to be adopted depends on the acceptable (permitted) voltage value across the semiconductor switches and the acceptable peak current value for the S_1 switch.

Combining the aforementioned remarks, the transformer turns ratio must be selected between 0.2 and 2.8 in Europe and between 0.3 and 5.5 in USA. This selection limits the maximum voltage across the semiconductor switches under 1 kV and the maximum peak current through the primary switch S_1 at the very most ten times higher than the average value of the primary transformer winding current. In this way, the meaning of the term "acceptable n area for Europe," which is shown in Fig. 5, is clarified.

IV. Basic Analysis of the BCM Operation

The new operation scheme that is introduced for PV applications in this paper, leads the inverter to the boundary between continuous and DCM of operation. Thus, the switching frequency necessarily varies during a line half cycle to achieve complete transformer discharge without any time intervals of zero transformer current flow. So, for the case of BCM operation, a variable switching frequency (VSF) control technique must be applied.

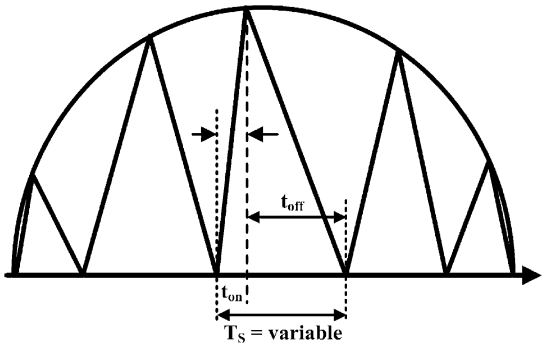

Fig. 7. Transformer current representation for the case of BCM operation (variable switching frequency).

The basic equations for the BCM scheme can be derived by an analysis similar to the previous case. The equivalent transformer current waveform for this case is shown in Fig. 7.

Obviously, the main difference between this mode of operation and the DCM scheme is that, in BCM, a new switching cycle begins each time the transformer current reaches zero

$$T_s(t) = t_{\rm on}(t) + t_{\rm off}(t). \tag{30}$$

During $t_{\rm on}$, the equivalent circuit is that of Fig. 2(b), and so, the peak current value can be described by (4). Since the peak current waveform should be a sinusoidal one, the $t_{\rm on}$ interval should be modified as

$$t_{\rm on}(t) = t_{{\rm on},p} \sin \omega t \tag{31}$$

where $t_{{\rm on},p}$ is the $t_{\rm on}$ interval value referring to the switching cycle that occurs at the time-area of $\omega t = \pi/2$.

Additionally, Fig. 2(b) and (10) stand for the description of the off-time interval. So, $t_{\rm off}$ becomes

$$t_{\rm off} = \frac{\lambda}{n} t_{{\rm on},p} = \text{constant} \tag{32}$$

for each switching cycle.

Finally, according to (30)–(32), the switching period value can be expressed as

$$T_s(t) = t_{\rm on}(t) + t_{\rm off} = \left(\frac{\lambda}{n} + \sin \omega t\right) t_{{\rm on},p}. \tag{33}$$

According to (33), the maximum and minimum switching frequency values—during a line half cycle—are

$$f_{s,\max} = \frac{1}{T_{s,\min}} = \left.\frac{1}{T_s}\right|_{\omega t = 0} = \frac{n}{\lambda\, t_{{\rm on},p}} \tag{34}$$

$$f_{s,\min} = \frac{1}{T_{s,\max}} = \left.\frac{1}{T_s}\right|_{\omega t = \frac{\pi}{2}} = \frac{1}{\left(\frac{\lambda}{n} + 1\right) t_{{\rm on},p}}. \tag{35}$$

Fig. 8 shows the block diagram for the BCM scheme.

Since the switching frequency varies, a variable frequency control technique is applied. Contrary to DCM operation, the control loop is more complex since it demands sensing of both the primary and secondary transformer currents. Nevertheless, this more complicated control loop reassures that the circuit will not enter continuous conduction mode (CCM) region under any condition, because the beginning of a new switching cycle demands the complete transformer discharge.

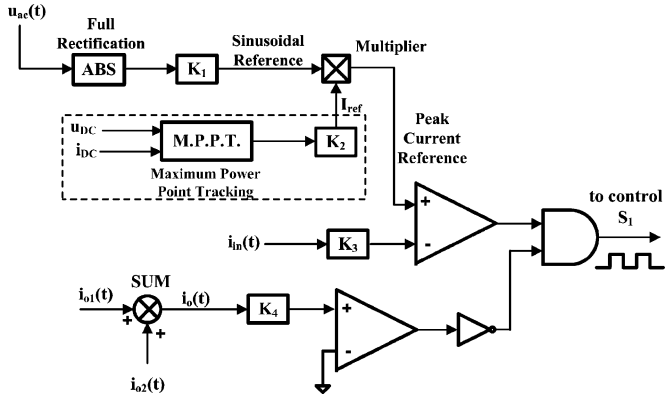

Fig. 8. Block diagram of the control circuit for the BCM operation (variable switching frequency).

A. Investigation of the Power Density for BCM

As discussed in the previous case, the transferred power will be calculated by using (15)–(18). Combining these equations with (31)–(33), we can express the transferred power as

$$P = \frac{1}{2}\frac{V_{\rm dc}^2}{L_1} t_{{\rm on},p} \left(\frac{1}{\pi}\int_0^{\pi} \frac{\sin^2\theta}{\left(\frac{\lambda}{n} + \sin\theta\right)} d\theta\right) = \frac{1}{2}\frac{V_{\rm dc}^2}{L_1} t_{{\rm on},p} F\left(\frac{\lambda}{n}\right). \tag{36}$$

In order to obtain an expression similar to the DCM case, the "average switching frequency" $f_{s,\rm avg}$ will be introduced

$$f_{s,\rm avg} = \frac{1}{T_{s,\rm avg}} \tag{37}$$

$$T_{s,\rm avg} = \frac{1}{\pi}\int_0^{\pi} {\rm T}_s(\theta) d\theta, \quad \theta = \omega t. \tag{38}$$

Combining (33), (37), and (38), $f_{s,\rm avg}$ becomes

$$f_{s,\rm avg} = \frac{1}{t_{{\rm on},p}} \frac{1}{\left(\frac{\lambda}{n} + \frac{2}{\pi}\right)}. \tag{39}$$

Furthermore, the function $F(\lambda/n)$ of (36) can be analytically calculated according to the following formula:

$$F\left(\frac{\lambda}{n}\right) = \frac{1}{\pi}\int_0^{\pi} \frac{\sin^2\theta}{\left(\frac{\lambda}{n} + \sin\theta\right)} d\theta = \frac{2}{\pi} - \frac{\lambda}{n} + \left(\frac{\lambda}{n}\right)^2 S\left(\frac{\lambda}{n}\right) \tag{40}$$

where (see Appendix C)

$$S\left(\frac{\lambda}{n}\right) = \frac{1}{\pi}\int_0^{\pi} \frac{d\theta}{\frac{\lambda}{n} + \sin\theta}$$

$$= \begin{cases} \frac{2}{\pi\sqrt{\left(\frac{\lambda}{n}\right)^2 - 1}} \arctan\sqrt{\left(\frac{\lambda}{n}\right)^2 - 1}, & \text{for } \frac{\lambda}{n} > 1 \\ \frac{2}{\pi}, & \text{for } \frac{\lambda}{n} = 1 \\ \frac{2}{\pi\sqrt{1 - \left(\frac{\lambda}{n}\right)^2}} \arctan h\sqrt{1 - \left(\frac{\lambda}{n}\right)^2}, & \text{for } \frac{\lambda}{n} < 1 \end{cases}. \tag{41}$$

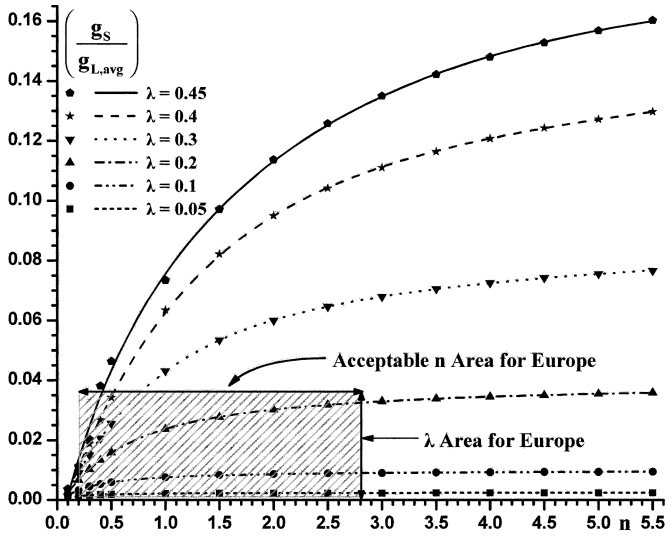

Fig. 9. $(g_S/g_{L,\mathrm{avg}})$ as a function of λ and n, for the BCM operation.

Using (12) and (36)–(41), the transferred power finally becomes

$$P = g_S V_{\mathrm{ac,rms}}^2 = g_{L,\mathrm{avg}} \frac{\lambda^2}{\left(\frac{\lambda}{n}+\frac{2}{\pi}\right)} \left[\frac{2}{\pi} - \frac{\lambda}{n} + \left(\frac{\lambda}{n}\right)^2 S\left(\frac{\lambda}{n}\right)\right] V_{\mathrm{ac,rms}}^2 \quad (42)$$

leading to the following relation between g_S and $g_{L,\mathrm{avg}}$:

$$\frac{g_S}{g_{L,\mathrm{avg}}} = \frac{\lambda^2}{\left(\frac{\lambda}{n}+\frac{2}{\pi}\right)} \left[\frac{2}{\pi} - \frac{\lambda}{n} + \left(\frac{\lambda}{n}\right)^2 S\left(\frac{\lambda}{n}\right)\right] \quad (43)$$

where

$$g_{L,\mathrm{avg}} = \frac{1}{f_{s,\mathrm{avg}} L_1}. \quad (44)$$

Fig. 9 shows $(g_S/g_{L,\mathrm{avg}})$ as a function of n with λ as a parameter. Comparing with Fig. 5, the power transfer that can be achieved in this mode of operation is significantly higher than that of the DCM operation for the same values of λ and n; the power transfer limit for this case is given by

$$\left.\frac{g_S}{g_{L,\mathrm{avg}}}\right|_{n\to\infty} = \lambda^2. \quad (45)$$

A comparison between (45) and (26) shows that using BCM operation (assuming g_L and $g_{L,\mathrm{avg}}$ have similar values), the power transfer becomes twice the maximum power transfer of the DCM operation. Therefore, the use of BCM instead of DCM mode, for a specific power level, leads to a transformer volume decrease of approximately 50%. This important advantage highlights that BCM is the most suitable mode of operation for the development of reduced-size efficiency-effective ac–PV modules inverter.

After the basic theoretical analysis of the BCM operation, it is essential to investigate the influence of the parameters λ and n in this operation scheme. Since the switching frequency

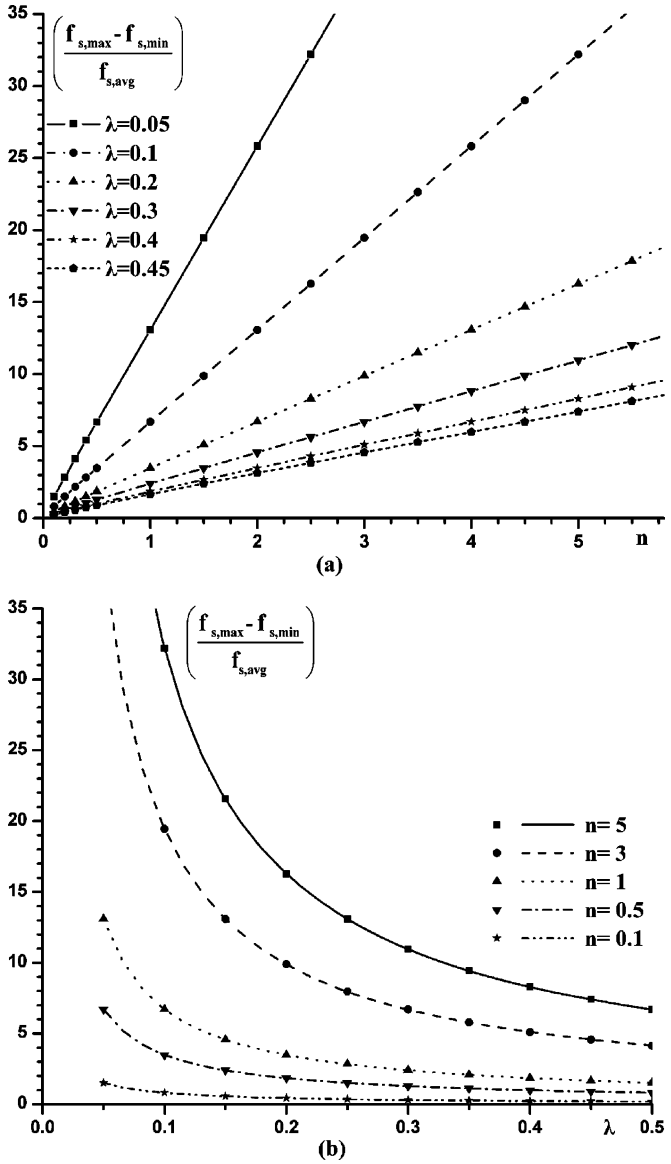

Fig. 10. Ratio of switching frequency bandwidth and $f_{s,\mathrm{avg}}$ as a function of n and λ for the BCM operation. Switching frequency bandwidth as function of (a) n with λ as a parameter and (b) λ with n as a parameter.

of the switch at the PV generator side is not constant, there is another limitation concerning the values of λ and n; in Fig. 10(a), the switching frequency bandwidth is shown as a function of n with λ as parameter. Apparently, for a given λ, as the value of n increases, the switching frequency bandwidth also increases, and $f_{s,\max}$ becomes significantly higher than $f_{s,\min}$ (especially for practical λ-values in PV applications). The above remark infers that the selection of the transformer turns ratio significantly affects the selection of the upper and lower limit of the switching frequency, and so, the design of the inverter as well as the design of the output filter becomes more complicated. Additionally, the upper limit of the switching frequency ought to assure that the semiconductor switches will operate within their safe operation area.

Furthermore, in a real system, the value of λ varies because the irradiation and the ambient temperature changes affect the PV

output voltage. Analytically, for a given transformer turns ratio, as it is shown in Fig. 10(b), a PV generator voltage decrease also leads to a switching frequency bandwidth increase (especially for high n values), thereby limiting the use of BCM scheme according to the aforementioned remarks.

Last but not least, the maximum permitted peak current value of the primary switch S_1 is effected by the $t_{\mathrm{on},p}$ value, according to (4). Additionally, the average switching frequency of the main switch S_1 depends also on the selection of $t_{\mathrm{on},p}$. In more detail, $f_{s,\mathrm{avg}}$ is a function of $t_{\mathrm{on},p}$ as shown in (39). Taking into account (34), the adopted value of $t_{\mathrm{on},p}$ has to reassure that the semiconductor switch S_1 will operate within its safe operation area for the maximum switching frequency. So, a compromise among $f_{s,\mathrm{avg}}$, $f_{s,\mathrm{max}}$, and the maximum peak current values has to be made.

V. Comparison Between DCM and BCM

Following the theoretical analysis, a comparison between BCM and DCM modes is given in this section. The most important conclusions can be summarized to the following remarks.

- BCM is the only feasible solution for high-power levels.
- The control loop in BCM is more complicated than in DCM—since it demands the sensing of both transformer current parts. However, the fact that the transformer has to be completely discharged before the beginning of a new switching cycle reassures that the inverter will not enter CCM. The sensing of both transformer current parts can be realized with the usage of current transformers, similar to current-mode control, peak current control, and current limiting applications, since both currents have appropriate high-frequency switching waveforms [19]–[21]. The use of current transformers is particularly useful because galvanic isolation is achieved between the measured quantity and the control circuit, while the short-circuit current is limited. Finally, the total control circuit cost significantly decreases due to the usage of these inexpensive current sensors.
- DCM has a very simple control loop. This fact reduces the total cost, establishing it as an attractive solution for low-power PV applications. Its small power process capability limits its use at a lower power range compared to BCM for a given volume.
- The fact that the transformer current is not measured may lead—under heavy load or transient conditions—the inverter in continuous conduction, and so, a short circuit will take place. Thus, the inverter should be very carefully designed in order to reassure that under any circumstances it will not enter CCM.
- The irradiation and the ambient temperature changes affect both DCM and BCM operation, leading to diminished transfer power, due to the PV generator voltage decrease. Despite this fact, in DCM operation (where the switching frequency is constant), the mains current harmonic content is not affected by the aforementioned changes.
- In BCM operation, the filter design is more complicated in general, since it has to cutoff frequency values that depend on line and load conditions. On the contrary, the filter is less distressed compared to DCM operation, since the harmonic content is distributed in a large frequency range. So, BCM operation presents smaller THD than DCM [19].

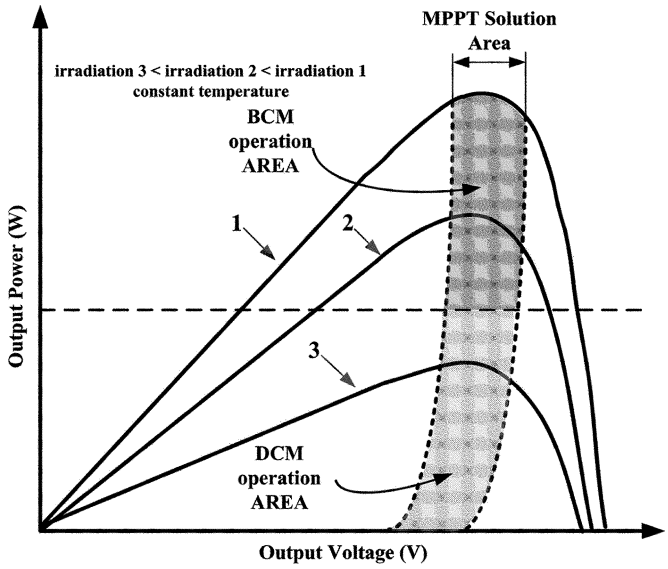

Fig. 11. Typical power characteristic for a solar module; proposed control strategy for an ac–PV module.

According to the earlier remarks, it is obvious that the control loop in BCM mode is more complicated; however, this control loop does not lead to any significant cost increase (compared to the DCM control loop) since inexpensive current transformers are used. Considering that the use of current transformers limits short-circuit currents and that the transformer volume increase is insignificant, we conclude that practically, without any cost increase, the use of BCM operation doubles the inverter-processed power.

The increase of the electric power per unit square meter of a PV cell module, due to the different solar cell technologies, establishes BCM scheme as the most appropriate mode for PV applications with the smallest possible volume. Fig. 11 shows a typical power characteristic of a solar module for constant temperature and varying irradiation.

Any PV power decrease (due to irradiation decrease) calls for a decrease in $t_{\mathrm{on},p}$ value; so, the average switching frequency as well as the upper and lower frequency limits take considerably higher values than the rated ones. Thus, BCM operation is suitable for power levels greater than a certain limit, as shown in Fig. 11. For lower power levels, DCM operation is used in order to exploit all the available PV generation. Moreover, this combination of BCM and DCM operation, proposed in this paper, establishes the flyback inverter as a global solution for "ac–PV module" applications for wide power range.

VI. Design Procedure for Optimal Power Transfer Density

For low-power level PV applications, DCM is the most attractive solution according to the aforementioned remarks. In these

applications, aiming for an inverter with the smallest possible volume, the following design procedure has to be adopted.

1) For given values of mains voltage, as well as PV generator maximum power and dc voltage, the value of λ parameter is calculated by (12).
2) Taking into account the remarks that have been mentioned for the transformer turns ratio in Section III-A, we select the n-value so as to lead the inverter within the "safe operational frame" of Fig. 5, while keeping its power density (g_S/g_L) as high as possible for the specific λ-case.
3) From (13), we can calculate the value of d_p which reassures that under any circumstances, the inverter will be able to remain in the DCM operation.
4) Assuming that the inverter has unitary efficiency, the maximum power transferred to the network is equal to the PV maximum power, and so, according to (23), the current-source conductivity g_S can be calculated.
5) Afterwards, the g_L-value can be derived from (25) by using the adopted n-value and the calculated current-source conductivity. It is worth mentioning that this g_L-value is selected such that g_S/g_L becomes maximum for the specific λ and n values, as shown in Fig. 5.
6) By substituting the result of (25) into (20), we obtain an expression for the product of the transformer primary inductance and the switching frequency of the semiconductor switch S_1. Finally, we can calculate the transformer primary inductance by selecting the desired switching frequency of the S_1. Certainly, the selected switching frequency has to guarantee that S_1 will operate within its safe operation area.

However, for higher power level PV applications, BCM is the only feasible solution (as it has been shown in Section IV). On the other hand, a considerable irradiation decrease, and consequently, a PV-generated power decrease limits the use of BCM due to the switching frequency bandwidth increase (as it has been shown in Section IV-A). Thus, in such applications, a combination of BCM and DCM operation should be adopted in order to exploit all the available PV generation. This combination claims for the following generalized design procedure.

First of all, the inverter operational parameters are calculated for the case of BCM operation.

1) Concerning the calculation of the current-source conductivity value, the parameter λ, and the appropriate selection of the transformer turns ratio (taking also into account its limitation by the maximum permitted voltage value across the semiconductor switches), the comments that have been mentioned for low-power level PV applications should be considered. For these calculations, the given value of the mains voltage and the maximum values of PV generator power and dc voltage should be used.
2) The $g_{L,\mathrm{avg}}$-value is derived from (43) by using the adopted n-value and the calculated current-source conductivity. It is worth mentioning that this $g_{L,\mathrm{avg}}$-value is selected such that $g_S/g_{L,\mathrm{avg}}$ becomes maximum for the specific λ and n values, as shown in Fig. 9.
3) Replacing the result of (43) into (44), an expression for the product of the transformer primary inductance with the average switching frequency of the semiconductor switch S_1 is derived.
4) Finally, we can calculate the transformer primary inductance by selecting the congruent average switching frequency of S_1, taking into account the remarks that were mentioned for the $t_{\mathrm{on},p}$ in Section IV-A.

Thereafter, the lower power limit for the BCM operation should be defined. From (36), (34), and the chosen value of L_1, the power level wherefore $t_{\mathrm{on},p}$ leads to unacceptable $f_{s,\max}$ value is derived. In this way, the lower safe power level for the semiconductor switch S_1 is determined. Actually, the use of this mode of operation should be signed off shortly before this power level. The transition between BCM and DCM takes effect in this region, in order to exploit the lower PV generation.

Finally, the safe use of DCM depends on the judicious selection of $d_p, f_S, i_{dc,p}$. For this PV generator power level, the steps 3–6 of the DCM design procedure have to be performed. Thus, the new current-source conductivity is determined, and the aforementioned parameters can be calculated. Last but not least, the above calculations are acceptable, if the resulting $i_{\mathrm{dc},p}$ value does not lead to excessive peak currents and the resulting f_S guarantees that S_1 will operate within its safe operation area. Otherwise, a redefinition of L_1 value is required.

The aforementioned design methodology assures the smallest possible inverter volume for wide power transfer to the public grid.

VII. Simulation and Experimental Results

The inverter operation in the proposed BCM mode was experimentally examined on a 200-W laboratory prototype for the case of a PV generator with 50-V constant dc voltage, 200-W maximum power, and 220-V_{rms}, 50-Hz mains voltage. The inverter operation in the DCM scheme was examined on a 100-W laboratory prototype and also with personal computer simulation program with integrated circuit emphasis (PSPICE) simulation results for the same values of PV generator voltage, λ parameter, and transformer primary inductance values in order to prove that in BCM, the power transfer that can be achieved is significantly higher than that of the DCM.

For both modes of operation, the inverter is studied without the presence of MPPT control, since the aim of this paper is to investigate the design procedure under any line and load conditions.

Considering (12) and (23), the value of λ is equal to 0.16, and the value of the current-source conductivity is equal to 4.132 $\mathrm{m}\Omega^{-1}$ (the maximum power that is transferred to the network is 200 W). According to the design procedure that was presented in the aforementioned sections, for the case of BCM operation, the transformer turns ratio is selected to be 0.5. The parameters, which lead to this n-value, are an acceptable (maximum) voltage value across the semiconductor switches ($V_{s1,p} \approx 200$ V, $V_{s2,p} \approx 720$ V), an acceptable maximum peak current value, and the selection of a ferrite core with a small volume. Taking for granted that the leakage of the transformer is not zero, the use of a 500-V MOSFET (for the low-voltage stage switch S_1) is the cost-effective solution in our case. The ferrite

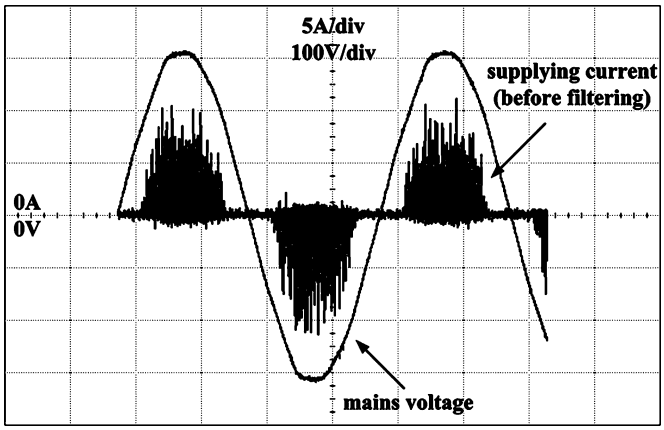

Fig. 12. Supplying current waveform at the inverter mains side (before filtering) for the case of DCM operation (experimental results).

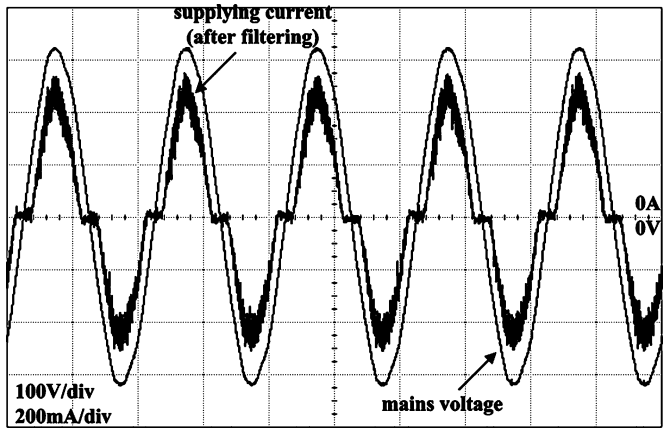

Fig. 13. Supplying current waveform at the inverter mains side (after filtering) for the case of DCM operation (experimental results).

core that has been selected is E42/21/15. The number of turns for the transformer primary winding is 29, while the number of turns for the transformer secondary winding is 58. Combining (41), (43), and (44), the selected average switching frequency of the semiconductor switch S_1 is 32 kHz, and the transformer primary inductance L_1 is 85 μH. Furthermore, the$t_{\mathrm{on},p}$ is 32.3 μs, and therefore, the maximum and minimum switching frequencies are 96 and 23 kHz, respectively. Finally, the maximum peak current value of the primary switch S_1 is 18 A, which is an acceptable value for the inverter power range.

For the case of DCM, taking into account that the maximum power transferred to the network is 100 W, from (23), the value of the current-source conductivity is equal to 2.066 mΩ^{-1}. Combining (20) and (25), and considering that $L_1 = 85$ μH and $n = 0.5$, as for the case of BCM, the switching frequency of the semiconductor switch S_1 is 40 kHz. Equation (13) shows that, in order to reassure that the inverter will not enter CCM, the value of d_p must be smaller than 0.76. So, the maximum peak current value of the primary switch S_1 is approximately 10 A.

Figs. 12 and 13 show the experimental inverter main current waveform before and after filtering, for the case of 100-W constant active power transfer at the mains side and 50-V PV generator voltage (DCM operation). Measurements were obtained by using the oscilloscope spectrum analyzer "HP infinium Oscilloscope 500 MHz 3 Gsa/s" and the current probe amplifier "Tektronix AM 503 B."

Furthermore, Fig. 14 shows the active power transfer P as a function of d_p, in comparison with the corresponding theoretical and PSPICE simulation values. By studying these results, we can conclude that the theoretical analysis is quite accurate, since the divergence among the simulation and experimental results and the corresponding theoretical values is slight.

Moreover, Figs. 15 and 16 show the inverter efficiency eff as well as the power factor pf as a function of the transferred power at the mains side P_{ac}, showing that the proposed inverter topology presents very high efficiency and power factor regulation even under light load conditions. Simulation and experimental results are very close due to the accurate models of the switching devices that were used in PSPICE and due to the fact that the switching frequency does not exceed 40 kHz. Obviously,

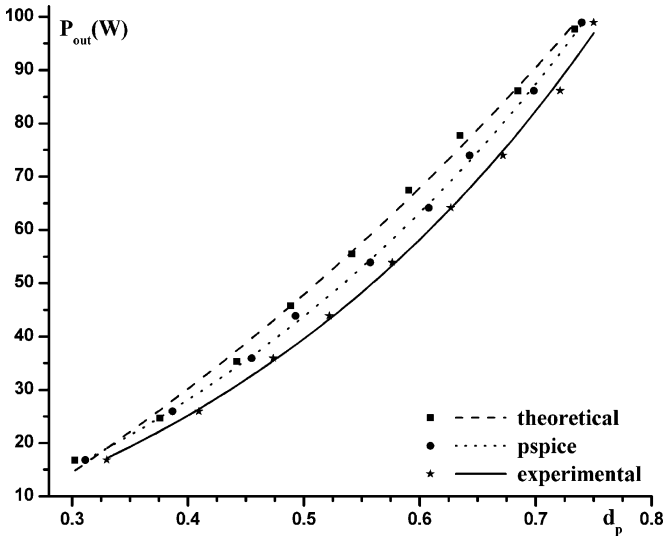

Fig. 14. Transferred power as a function of d_p for the DCM operation (theoretical values, simulation, and experimental results).

if the switching frequency increases beyond 100 kHz, the expected divergence between simulation and experimental results increases too.

Figs. 17 and 18 show the experimental inverter main current waveform before and after filtering, for the case of 200-W constant active power transfer at the mains side and 50-V constant PV generator voltage (BCM operation). These experimental results confirm the theoretical analysis in Section IV-A. For the same transformer volume, the power that can be processed by the inverter is doubled in the BCM mode compared to the one in DCM case.

Fig. 19 shows the harmonic content of the supplying current for the case of 200-W constant active power transfer at the mains side. This figure shows that the proposed inverter topology presents very high-power factor regulation and very low total harmonic distortion (the third harmonic content is already 28.75 db lower than the fundamental harmonic).

Furthermore, Fig. 20 shows the inverter efficiency eff as a function of the transferred power at the mains side P_{ac} for BCM

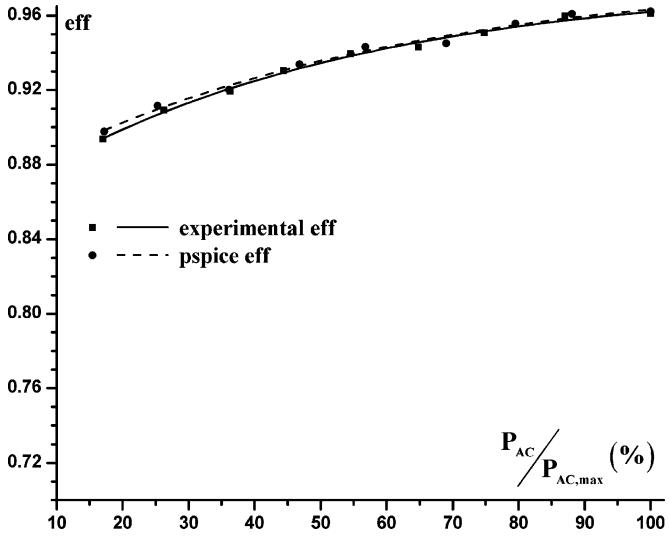

Fig. 15. Inverter efficiency as a function of the transferred power level for DCM operation (simulation and experimental results).

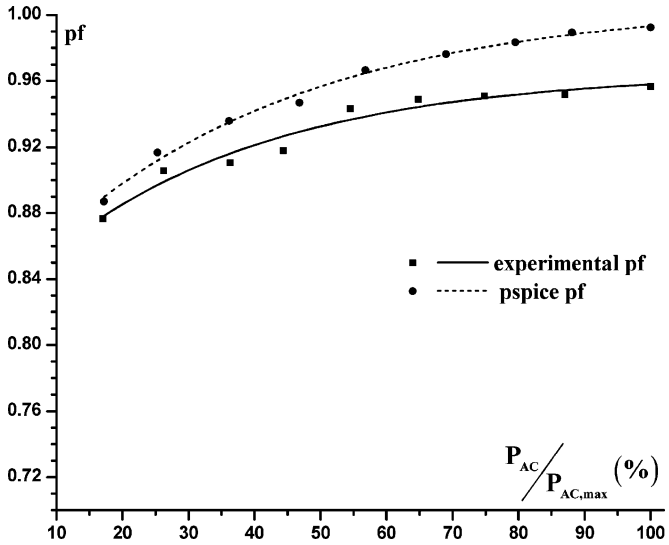

Fig. 16. Inverter power factor as a function of the transferred power level for DCM operation (simulation and experimental results).

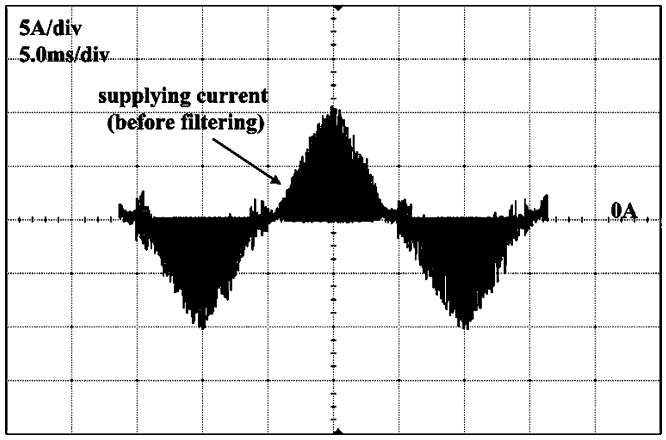

Fig. 17. Supplying current waveform at the inverter mains side (before filtering) for the case of BCM operation (experimental results).

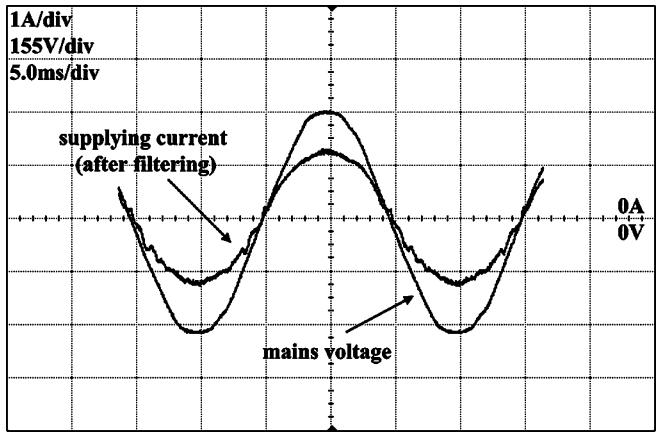

Fig. 18. Supplying current waveform at the inverter mains side (after filtering) for the case of BCM operation (experimental results).

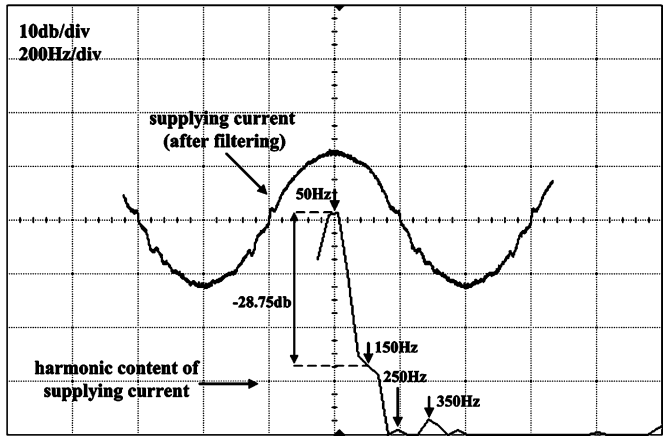

Fig. 19. Harmonic content of the supplying current at the inverter mains side for the case of BCM operation (experimental results).

and DCM operation, respectively, showing that the proposed inverter topology presents very high efficiency in both modes of operation but the transfer capability is quite higher in BCM. In the following section, the meaning of the terms "BCM effective area" and "DCM effective area," which are shown in this figure will be explained.

In order to achieve an inverter with the smallest possible volume for 200-W transferred power at the mains side, BCM technique is the advisable solution according to the analysis that was presented in the preceding sections. As transferred power decreases, the average switching frequency as well as the upper and lower frequency limits take considerably higher values than the rated ones according to Fig. 10.

So, the switching frequency bandwidth as well as the switching losses (as a percentage of the generated power) will increase. This fact limits the use of BCM operation beyond the power level of 100 W for the case of the specific experimental inverter. In order to exploit the available PV generation under 100 W, while keeping high efficiency, DCM technique must be applied. This proposed scheme can be used in general for any PV application. The exact border between BCM and DCM operation depends on the specific application and the designer's requirements (frequency bandwidth, efficiency, n-value selection, etc.)

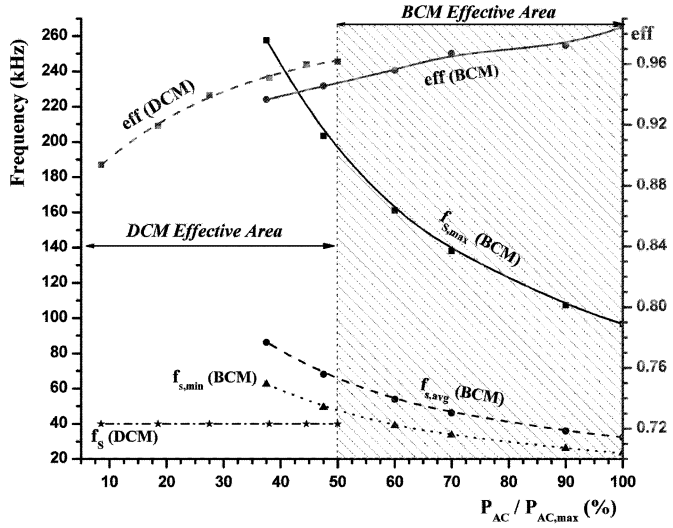

Fig. 20. Inverter efficiency (experimental results) and switching frequency bandwidth (theoretical results), as a function of the transferred power level for BCM and DCM operation ($P_{\mathrm{ac,max}}$ is equal to 200 W).

VIII. Conclusion

Two alternative modes of operation for the current-source flyback inverter for decentralized grid-connected PV systems have been investigated and compared. A design strategy for both the operation schemes has been proposed in order to achieve high-power density. Moreover, this paper has highlighted, both theoretically and experimentally, the optimum inverter behavior when these two modes of operation are combined, leading to a global and high-efficiency solution for wide power range "ac–PV module" applications.

Appendix A

According to Figs. 2(c) and 3, t_{off} interval can be calculated by using the following equation:

$$t_{\mathrm{off}} = \frac{n i_{\mathrm{dc},p}(t)}{u_{\mathrm{ac}}(t)}\frac{L_1}{n^2} = \frac{I_{\mathrm{dc},p}\sin\omega t}{V_{\mathrm{ac},p}\sin\omega t}\frac{L_1}{n} = \frac{I_{\mathrm{dc},p}}{V_{\mathrm{ac},p}}\frac{L_1}{n} \tag{A1}$$

where $n i_{\mathrm{dc},p}(t)$ is the peak secondary current value and L_1/n^2 is the secondary inductance value.

Taking into account that

$$t_{\mathrm{on}} = T_s d(t) = T_s d_p \sin\omega t \tag{A2}$$

$$I_{\mathrm{dc},p} = \frac{V_{\mathrm{dc}}}{L_1} t_{\mathrm{on},p} = \frac{V_{\mathrm{dc}}}{L_1 f_S} d_p. \tag{A3}$$

(A1) can be rewritten as

$$t_{\mathrm{off}} = \frac{V_{\mathrm{dc}} d_p}{L_1 f_S V_{\mathrm{ac},p}}\frac{L_1}{n} = \frac{\lambda}{n} d_p T_S.$$

So, we conclude

$$\frac{t_{\mathrm{off}}}{T_S} = \frac{\lambda}{n} d_p = \text{constant}$$

for any period within the line half cycle when λ remains constant.

Appendix B

$$i_{\mathrm{dc}}(t_x) = \frac{i_{\mathrm{dc},p}}{t_{\mathrm{on}}} t_x = \frac{I_{\mathrm{dc},p}\sin\omega t}{t_{\mathrm{on}}} t_x = \frac{V_{\mathrm{dc}}}{L_1 f_s}\frac{d_p \sin\omega t}{T_s d_p \sin\omega t} t_x = \frac{V_{\mathrm{dc}}}{L_1 f_s T_s} t_x \tag{B1}$$

where $t_x = t - (i-1)T_s, i = 1, 2, 3\ldots$

$$\int_{(i-1)T_s}^{T_s} i_{\mathrm{dc}}(t)\mathrm{d}t = \int_0^{t_{\mathrm{on}}} i_{\mathrm{dc}}(t_x)\mathrm{d}t_x = \frac{V_{\mathrm{dc}}}{L_1}\frac{t_x^2}{2}\bigg|_0^{t_{\mathrm{on}}} = \frac{V_{\mathrm{dc}}}{L_1}\frac{t_{\mathrm{on}}^2}{2} \tag{B2}$$

$$t_{\mathrm{on}} = T_s d_p \sin\omega t = T_s d_p \sin\omega i T_s \approx T_s d_p \sin\frac{\pi}{w} i. \tag{B3}$$

Due to the above equations, (17) can be rewritten as

$$I_{\mathrm{dc,avg}} = \frac{T_S}{T_{hl}}\frac{d_p^2 V_{\mathrm{dc}}}{2 f_s L_1}\sum_{i=1}^{w}\sin^2\left(\frac{\pi}{w} i\right) = \frac{d_p^2 V_{\mathrm{dc}}}{2 f_s L_1}\frac{1}{w}\sum_{i=1}^{w}\sin^2\left(\frac{\pi}{w} i\right) \tag{B4}$$

where

$$\begin{aligned}\frac{1}{w}\sum_{i=1}^{w}\sin^2\left(\frac{\pi}{w} i\right) &= \frac{1}{w}\sum_{i=1}^{w}\left[\frac{1}{2} - \frac{1}{2}\cos\left(\frac{2\pi}{w} i\right)\right] \\ &= \frac{1}{2} - \frac{1}{2w}\left\{\frac{\sin\left[\left(w+\frac{1}{2}\right)\frac{2\pi}{w}\right]}{2\sin\frac{2\pi}{2w}} - \frac{1}{2}\right\} \\ &= \frac{1}{2} - \frac{1}{4w}\left[\frac{\sin\left(2\pi + \frac{\pi}{w}\right)}{\sin\frac{\pi}{w}} - 1\right] \\ &= \frac{1}{2} - \frac{1}{4w}\left[\frac{\sin\frac{\pi}{w}}{\sin\frac{\pi}{w}} - 1\right] = \frac{1}{2}.\end{aligned} \tag{B5}$$

Appendix C

For $\dfrac{\lambda}{n} > 1$

$$\begin{aligned}S\left(\frac{\lambda}{n}\right) &= \frac{1}{\pi}\int_0^{\pi}\frac{d\theta}{\frac{\lambda}{n} + \sin\theta} \\ &= \frac{1}{\pi}\frac{2}{\sqrt{\left(\frac{\lambda}{n}\right)^2 - 1}}\arctan\left(\frac{\left(\frac{\lambda}{n}\right)\tan\left(\frac{\theta}{2}\right) + 1}{\sqrt{\left(\frac{\lambda}{n}\right)^2 - 1}}\right)\Bigg|_0^{\pi} \\ &= \frac{2}{\pi\sqrt{\left(\frac{\lambda}{n}\right)^2 - 1}}\left[\frac{\pi}{2} - \arctan\left(\frac{1}{\sqrt{\left(\frac{\lambda}{n}\right)^2 - 1}}\right)\right] \\ &= \frac{2}{\pi\sqrt{\left(\frac{\lambda}{n}\right)^2 - 1}}\operatorname{arc\,cot}\left(\frac{1}{\sqrt{\left(\frac{\lambda}{n}\right)^2 - 1}}\right)\end{aligned}$$

$$= \frac{2}{\pi\sqrt{\left(\frac{\lambda}{n}\right)^2 - 1}} \arctan \sqrt{\left(\frac{\lambda}{n}\right)^2 - 1}. \quad \text{(C1)}$$

For $\frac{\lambda}{n} = 1$

$$S\left(\frac{\lambda}{n}\right) = \frac{1}{\pi}\int_0^{\pi} \frac{d\theta}{\frac{\lambda}{n} + \sin\theta} = -\tan\left(\frac{\pi}{4} - \frac{\theta}{2}\right)\Big|_0^{\pi} = \frac{2}{\pi}. \quad \text{(C2)}$$

For $\frac{\lambda}{n} < 1$

$$S\left(\frac{\lambda}{n}\right) = \frac{1}{\pi}\int_0^{\pi} \frac{d\theta}{\frac{\lambda}{n} + \sin\theta}$$

$$= \frac{1}{\pi}\frac{1}{\sqrt{1-\left(\frac{\lambda}{n}\right)^2}} \ln\left(\frac{\left(\frac{\lambda}{n}\right)\tan\left(\frac{\theta}{2}\right) + 1 - \sqrt{1-\left(\frac{\lambda}{n}\right)^2}}{\left(\frac{\lambda}{n}\right)\tan\left(\frac{\theta}{2}\right) + 1 + \sqrt{1-\left(\frac{\lambda}{n}\right)^2}}\right)\Bigg|_0^{\pi}$$

$$= \frac{1}{\pi\sqrt{1-\left(\frac{\lambda}{n}\right)^2}} \ln\left(\frac{1 + \sqrt{1-\left(\frac{\lambda}{n}\right)^2}}{1 - \sqrt{1-\left(\frac{\lambda}{n}\right)^2}}\right)$$

$$= \frac{2}{\pi\sqrt{1-\left(\frac{\lambda}{n}\right)^2}} \operatorname{arctan}\, h\sqrt{1-\left(\frac{\lambda}{n}\right)^2}. \quad \text{(C3)}$$

REFERENCES

[1] S. Rahman, M. A. Kallat, and B. H. Chowdhury, "A discussion on the diversity in the applications of photovoltaic systems," *IEEE Trans. Energy Convers.*, vol. 3, no. 4, pp. 738–746, Dec. 1998.

[2] W. T. Jewell and R. Ramakumar, "The history of utility-interactive photovoltaic generation," *IEEE Trans. Energy Convers.*, vol. 3, no. 3, pp. 583–588, Sep. 1988.

[3] P. D. Maycock, "Cost reduction in PV manufacturing; impact on grid-connected and building integrated markets," *Solar Energy Mater. Solar Cells*, vol. 47, no. 1–4, pp. 37–45, Oct. 1997.

[4] J. Gow and C. Manning, "Photovoltaic converter system suitable for use in small scale stand-alone or grid-connected applications," *Inst. Electr. Eng. Proc. -Electr. Power Appl.*, vol. 147, no. 6, pp. 535–543, Nov. 2000.

[5] R. H. Wills, F. E. Hall, S. J. Strong, and J. H. Wohlgemuth, "The ac photovoltaic module," in *Conf. Rec. 25th IEEE Photovoltaic Spec. Conf.*, Washington, DC, May 13–17, 1996, pp. 1231–1234.

[6] A. Lohner, T. Meyer, and A. Nagel, "A new panel-integratable inverter concept for grid-connected photovoltaic systems," in *Proc. IEEE Int. Symp. Ind. Electron.*, Warsaw, Poland, Jun. 17–20, 1996, vol. 2, pp. 827–831.

[7] S. B. Kjaer. (2002, Feb.). State of the art analysis for the 'SolcelleInverter' project. Aalborg Univ. Aalborg, Denmark., [Online]. Available: http://www.iet.auc.dk/˜sbk

[8] S. B. Kjaer, J. K. Pedersen, and F. Blaabjerg, "A review of single-phase grid-connected inverters for photovoltaic modules," *IEEE Trans. Ind. Appl.*, vol. 41, no. 5, pp. 1292–1306, Sep./Oct. 2005.

[9] A. Zuccato and L. Rossetto, "Understanding and complying with CISPR and IEC 1000 standards on EMC," presented at the Tut. Eur. Power Electron. Drives Conf., Trondheim, Norway, Sep. 1997.

[10] M. Nagao and K. Harada, "Power flow of photovoltaic system using buck-boost PWM power inverters," in *Proc. 1997 Int. Conf. Power Electron. Drive Syst.*, Singapore, May. 26–29, 1997, vol. 1, pp. 144–149.

[11] Y. Konishi, S. Chandhaket, K. Ogura, and M. Nakaoka, "Utility-interactive high-frequency flyback transformer linked solar power conditioner for renewal energy utilizations," in *Proc. 2001 Int. Conf. Power Electron. Drive Syst.*, Bali, Indonesia, Oct. 22–25, 2001, pp. 628–632.

[12] T. Shimizu, K. Wada, and N. Nakamura, "A flyback-type single phase utility interactive inverter with low-frequency ripple current regulation on the dc input for an ac photovoltaic module system," in *Proc. IEEE Power Electron. Spec. Conf.*, Cairns, Australia, Jun. 23–27, 2002, vol. 3, pp. 1483–1488.

[13] N. P. Papanikolaou, E. C. Tatakis, A. Ciritsis, and D. Klimis, (2003, Sep. 2–4), Simplified high frequency converters in decentralized grid-connected PV systems: A novel low-cost solution. *Proc. 9th Eur. Conf. Power Electron. Appl.,* Toulouse, France, [CD-ROM]. Nr. 200.

[14] N. Kasa, T. Iida, and C. Liang, "Flyback inverter controlled by sensorless current mppt for photovoltaic power system," *IEEE Trans. Ind. Electron.*, vol. 52, no. 4, pp. 1145–1152, Aug. 2005.

[15] D. P. Hohm and M. E. Ropp, "Comparative study of maximum power point tracking algorithms," *Progress Photovoltaics: Res. Appl.*, vol. 11, no. 1, pp. 47–62, Jan. 2003.

[16] W. Bower and M. Ropp. (2002). Evaluation of islanding detection methods for photovoltaic utility-interactive power systems. IEA-PVPS T5-09. [Online]. Available: http://www.iea-pvps.org

[17] G. A. Smith, P. A. Onions, and D. G. Infield, "Predicting islanding operation of grid connected PV inverters," *Inst. Electr. Eng. Proc.-Electric Power Appl.*, vol. 147, no. 1, pp. 1–6, Jan. 2000.

[18] A. C. Kyritsis, J. C. Kobougias, D. S. Klimis, and E. C. Tatakis. (2005, Apr. 13–16). Comparison between ac PV modules topologies for decentralised grid connected applications. *Proc. CIGRE Symp. Power Syst. Dispersed Gener.*, Athens, Greece, [CD-ROM]. Nr. 101.

[19] L. Rossetto, G. Spiazzi, and P. Tenti, "Control techniques for power factor correction converters," in *Proc. Power Electron., Motion Control' 94 Conf.*, Warsaw, Poland, Sep. 20–22, 1994, pp. 1310–1318.

[20] K. H. Billings, *Handbook of Switchmode Power Supplies*. New York: McGraw-Hill, 1989.

[21] M. Kwok-wai and L. Yim-shu, "Technique for sensing inductor and dc output currents of PWM dc–dc converter," *IEEE Trans. Power Electron.*, vol. 9, no. 3, pp. 346–354, May 1994.

A. Ch. Kyritsis (S'00) received the Dipl. degree in electrical engineering from the University of Patras, Rion-Patras, Greece, in 2003, where he is currently working toward the Ph.D. degree in renewable energy sources.

His current research interests include power quality improvement and renewable energy sources issues.

E. C. Tatakis was born in Alexandria, Egypt, in 1957. He received the Dipl. degree in electrical engineering from the University of Patras, Rion-Patras, Greece, in 1981, and the Ph.D. degree in applied sciences from the University of Brussels, Brussels, Belgium, in 1989.

He is currently an Associate Professor of power electronics and electrical machines in the Department of Electrical and Computer Engineering, University of Patras. His research interests include switch mode power supplies, resonant converters, power-factor correction, electrical drive systems, photovoltaic systems, educational methods on electrical machines, and power electronics.

Dr. Tatakis is a member of the European Electronics Association, the Sociètè Royale Belge des Electriciens, and the Technical Chamber of Greece.

N. P. Papanikolaou received the Dipl. Eng. and the Ph.D. degrees in electrical engineering from the University of Patras, Rion-Patras, Greece, in 1998 and 2002, respectively.

He is currently a special Scientific Staff Member with the Hellenic Transmission System Operator (HTSO) S.A., N. Smyrni, Greece, where he is engaged in power system analysis. His research has been concerned with power quality improvement issues.